Analyzing Gas Transport Phenomena in Secondary Pore of Washcoat Layer Determined by X-ray CT and Modelling

Satoru Kato*[a], Satoshi Yamaguchi[a], Takeshi Uyama[a], Toshitaka Tanabe[a], Yasutaka Nagai[a], Jota Yamauchi[b], Hiroshi Yamada[c], Tomohiko Tagawa[c]

a Toyota Central R & D Labs., Inc., 41-1 Yokomichi, Nagakute City, Aichi prefecture, 480-1192 Japan
b Toyota Motor Corporation., 1200, Mishuku, Shizuoka prefecture,410-1193 Japan
c Nagoya Univ. Dept. Chem. Eng., Hurocho, Chikusa Ku, Nagoya City, Aichi prefecture, 464-8603 Japan
e1325@mosk.tytlabs.co.jp

Washcoated catalysts on honeycomb substrates are widely used as automotive catalysts, and it is well known that their catalytic performance is limited by gas transport resistance. In order to reduce the gas transport resistance, understanding the relationship between gas transport and pore properties is essential. Since a washcoat layer consists of porous metal oxide particles (e.g., Al2O3), the washcoat layer has two types of pores: primary pores, which are located inside the porous metal oxide particles themselves, and secondary pores, which are located among the porous metal oxide particles. We recently studied the effect of secondary pore connectivity on gas permeability by synchrotron X-ray computed tomography. Based on the results, we proposed a new model to predict the effective gas permeability of a washcoat layer by using parameters of the pore connectivity; however, the pore properties did not vary enough for this model to be validated. Therefore, in this research, we attempted to validate the model using a wide range of pore properties. In order to access various pore properties, 8 real washcoat layers and 12 virtual 3D structures were used. The pore properties of the real washcoat layers were determined using synchrotron X-ray computed tomography. The pore properties varied more widely in this study than in our previous study, thus allowing the model to be validated.

1. Introduction

Automotive catalysts are prepared by washcoating a support material (e.g., Al_2O_3) on a honeycomb substrate. As shown in Fig. 1, the pores of the washcoat layer are classified into two types; primary pores, which are voids inside the secondary particles of the support material, and secondary pores, which are gaps among the secondary particles of the support material. In a catalytic converter, gases first diffuse through secondary pores and then through the primary pores to react with the noble metal particles loaded on the surface of the primary pores. Since the gas transport behavior influences the catalytic performance, study about gas transport phenomena in washcoat layer is important [e.g., Kato et al. (2013, 2015a and b)]. Thus the effect of the pore properties on the gas transport phenomena must be well understood to establish the design guide line for washcoat layer.
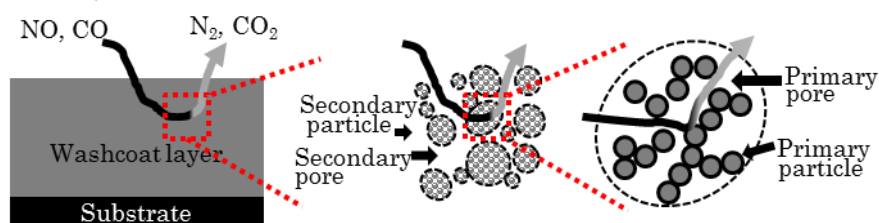

Fig. 1 Simple diagram of gas transport phenomena in washcoat layer

In our previous research [Kato et al. (2017)], the secondary pore connectivity of a washcoat layer was analyzed by X-ray computed tomography (CT) imaging. The gas transport properties were evaluated based on the gas permeability. The contribution of the primary pores to the total permeability can be neglected, as reported by Salejova et al. (2011). Although we developed a new model to describe the gas permeability in terms of the pore connectivity, the validity of the model could not be verified due to the lack of sample variety and the limited X-ray CT spatial resolution.

In this study, in order to validate our model, 8 real catalysts were used and 12 virtual 3D structures were computed. Virtual 3D structures are advantageous because they avoid the experimental problems of X-ray spatial resolution, and a wide range of pore properties can easily be obtained.

2. Experimental

2.1 Characterization

The secondary pores of washcoat layers for 8 real catalysts were observed. A cross-sectional micrograph of the washcoat layer was obtained by scanning electron microscopy (SEM). For the measurement, the catalyst was embedded in an epoxy resin. The fixed sample was cut and ground down to create a smooth surface to measure. The 3D structure of the washcoat layer was reconstructed from synchrotron X-ray CT imaging that was carried out at BL33XU of Spring-8, Japan Synchrotron Radiation Research Institute (JASRI) [Nonaka et al. (2016), Hirose (2009)]. A volume of $650 \times 650 \times 650$ µm^3 was imaged with 1800 projections and a photon energy of 29 keV. Tomographic reconstruction was achieved using software published by JASRI (http://www-bl20.spring8.or.jp/xct/). The voxel size of the resulting 3D image was 0.325 µm and the spatial resolution was approximately 0.65 µm. The pore morphology was extracted with the software package ExFact VR® and ExFact VR® Analysis Particle/Pore (Nihon Visual Science).

2.2 Computing virtual 3D structure

In order to verify the new model, it is necessary to prepare a series of samples that have a wide variation in their pore properties, such as pore size and porosity. A series of virtual 3D structures was computed by GeoDict® in addition to the above-mentioned 8 real samples. The virtual 3D structure consists of virtual particles. In our previous research, the secondary particle diameters of support material were in the range of 2 to 8 µm. Hence, virtual particles of 2, 4 and 6 µm in diameter were investigated. Binder for the virtual particles was investigated at levels of 0 and 10%. Porosities of 20% and 30% were investigated. A list of the virtual structures examined in this research is summarized in Table 1.

Table 1 List of virtual structures

Sample ID	Diameter of virtual particle (µm)	Binder (vol%)	Porosity (%)
1	2	0	20
2	2	0	30
3	4	0	20
4	4	0	30
5	6	0	20
6	6	0	30
7	2	10	20
8	4	10	20
9	6	10	20
10	2	10	30
11	4	10	30
12	6	10	30

Figures 2 and 3 show cross-sectional images of samples ID4 and ID11, respectively. In these figures, the grey area represents the material and the white area represents the secondary pores. Both ID4 (Fig. 2) and ID11 (Fig. 3) consist of virtual particles with a diameter of 4 µm, with a porosity of 30%, but their appearances differ. For ID 4, which does not include the binder, the particle shapes can be observed as shown in Fig. 2. For ID11, which includes the binder, the particle shapes are difficult to distinguish, as shown in Fig. 3. This is because the particles are connected by the binder. Generally, slurries for the washcoating process contain binders such as aluminum nitrate to prevent the support material from separating. The amount of binder depends on the properties of the support material, such as the size distribution of the secondary particles. In this research, ID1–ID6 represent no-binder cases, while ID7–ID12 represent cases in which a large amount of binder was used.
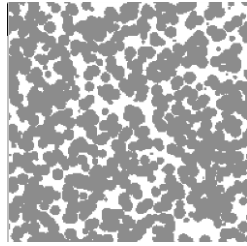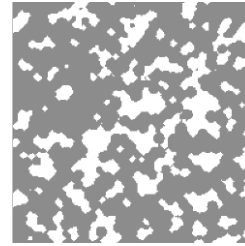
Fig. 2 Cross sectional image of ID4

Fig. 3 Cross sectional image of ID11

2.3 Calculating pore properties and effective permeation coefficients

SEM images were used to calculate porosity of secondary pore with the software package WinROOF (Mitani.co). For real and virtual 3D structures, properties of secondary pore such as porosity, pore size distribution and pore connectivity were determined with GeoDict®. The pore size distribution was determined by granulometry. The pore connectivity was evaluated by percolation path analysis, in which the percolation path was calculated by moving virtual spheres through the pores. The path size was defined as the diameter of the virtual largest sphere that could move through the path. The path length was determined by the trajectory of the moving sphere, and was calculated via the shortest route. The ratio of the path length and percolation length represents the tortuosity factor of the path.

Gas permeation in porous media can be described with Darcy law:

$$U = \frac{K_e}{\mu} \frac{\Delta P}{L}$$

(1)

where U is the superficial flow velocity (ms^{-1}), K_e is the effective permeation coefficient μ is the viscosity (Pa s), ΔP is the pressure drop (Pa) and L is the length over which the pressure drop takes place (m). Effective permeation coefficients of the virtual 3D structures could not be measured experimentally. Therefore, the effective permeation coefficient was calculated by computed fluid dynamics (CFD) with GeoDict®. By using CFD, it is possible to compare the real 3D structures with the virtual 3D structures. For the calculations, the Stokes solver (EJ method) with air at 20 ℃, a symmetric boundary condition, and an normalized non-dimensional accuracy of 0.1% were used.

3. Results and Discussion

3.1 Pore properties

In order to confirm that the resolution of the X-ray CT was sufficient for this study, the porosities calculated from the SEM images were compared with values calculated from the X-ray CT. The results are shown in Fig. 4. In our previous research [Kato et al. (2017)], the porosities calculated from X-ray CT were smaller than those calculated from SEM images by a factor of 1/3–3/4 because the resolution of the X-ray CT (0.325 μm/vox) was lower than the resolution of SEM (0.05 μm/pix). In this study, as shown in Fig. 4, X-ray CT yielded porosities similar to the values calculated from SEM. This may be because the pore sizes of the samples were larger than those used in our previous research. Thus, it was confirmed that the spatial resolution of the X-ray CT was sufficient for the 8 samples used in this research.
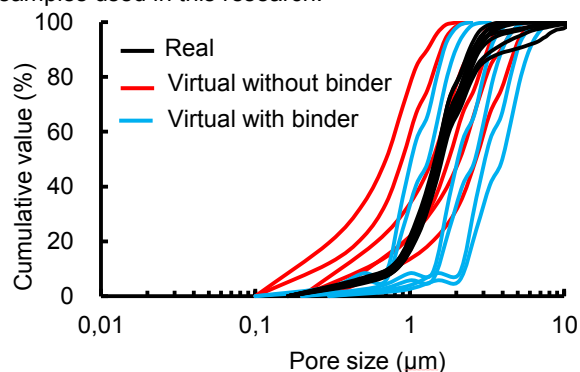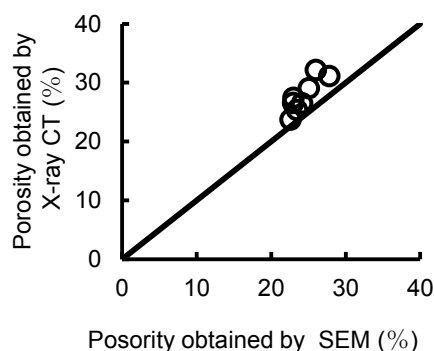

Fig. 4 Comparing porosities of X-ray CT and SEM   Fig. 5 Pore size distributions for 3D structures

Figure 5 shows the pore size distribution for real 3D structures experimentally determined with X-ray CT and computed virtual 3D structures. Y-axis in Fig. 5 represents the normalized cumulative pore size distributions. For the real 3D structures, similar pore size distributions were obtained whereas the pore size distributions for the virtual 3D structures covered a wide range with some similar to those of the real 3D structures. The average pore size, which is the 50% value in the cumulative curve, for real 3D structures is 1.6 – 1.8 μm. While a wide variation of average pore size for real 3D structures was not obtained, Saeki et al. (2002) reported that washcoats in actual catalysts can have variations in average pore size of 0.2 – 3 μm. A similar variation of average pore size was obtained with virtual 3D structures in the range of 0.7 – 4 μm.

The pore connectivity was evaluated by percolation path analysis. The results are shown in Fig. 6 and Fig. 7. In Fig. 6, path density is calculated by normalizing number of path with the cross sectional area of domain for calculating percolation path. In Fig. 7, the average tortuosity factor, which is the 50% value in the cumulative curve, is in the range of 1.3 – 1.6.

As shown in Fig. 5, the virtual 3D structures seemed to successfully simulate the real 3D structures from the point of view of the pore size distribution. However, Figs. 6 and 7 indicate a disadvantage of computing virtual 3D structures. In Fig. 6, the real 3D structure shows a path density between approximately 10^7 for larger path and 10^{12} smaller path (number of path / m^2). Their range is approximately 10^5 (number of path / m^2). However, for the case of the virtual 3D structure, range of path density between larger path and smaller path is approximately 10^2 (number of path / m^2). This means that the virtual 3D structure is simpler than the real 3D structure. This simplicity is also reflected in Fig. 7. Although 12 virtual 3D structures were evaluated, the cumulative curve represented only 4 types, indicating they were similar. This similarity of virtual 3D structures can be avoided by controlling the parameters for constructing the virtual 3D models. The size distribution of secondary particles may also need to be considered. These parameter studies may lead to a better understanding of the essence of the pores of washcoat layers and will be the subject of future work.
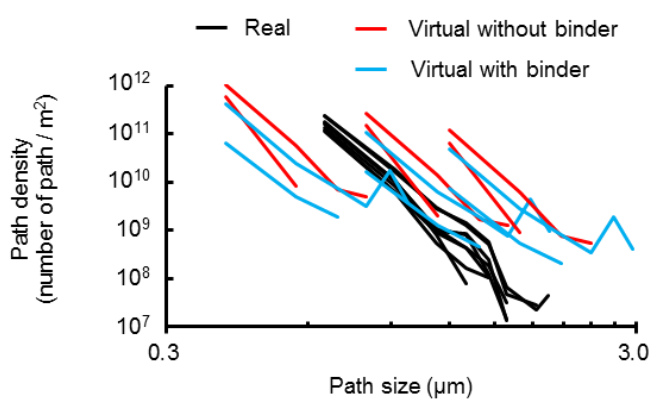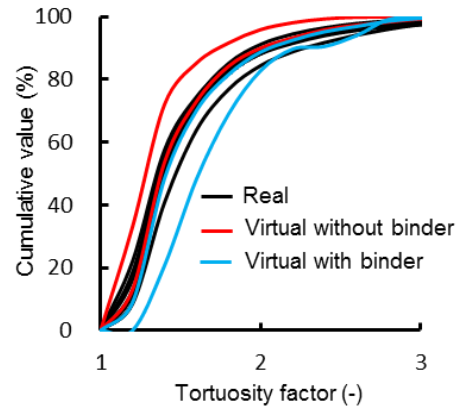

Fig. 6 Path size distribution

Fig. 7 Tortuosity factor distribution

3.2 Calculation of effective permeation coefficients with CFD

As shown in Fig. 8, the effective permeation coefficient calculated with CFD is in the range of 3.6×10^{-15} to 1.1×10^{-14} m^2 for real 3D structures (ID1-ID8), and for virtual 3D structures (ID1-ID12) it is in the range of 5.7×10^{-16} to 4.7×10^{-14} m^2.
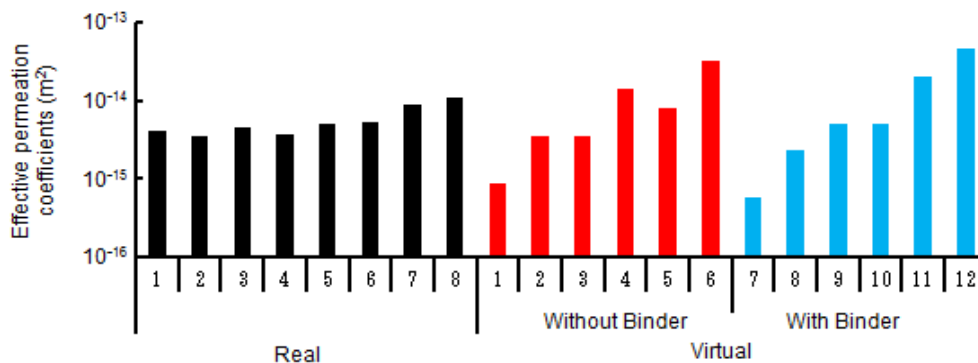

Fig. 8 Effective permeation coefficients

3.3 Verification of the new model

The effect of pore properties on gas transport properties is a fundamental issue in the study of transport phenomena in porous media. One popular method of evaluating the effective permeation coefficient is the Kozeny-Carman (K-C) equation [Kozeny et al. (1927) and Carman et al. (1937)]. This equation calculates the effective permeation coefficient over a very wide range due to the empirical factor. In our previous study [Kato et al. (2017)], since the empirical factor for the washcoat layer was not reported, the calculated effective permeation coefficient for the washcoat layer had a range of approximately 10^2 (m^2), which was too wide to discuss the effects of pore properties on effective gas permeability. Consequently, we focused on Miyakoshi's theoretical model (1989), which does not include an empirical factor. By modifying this model, we proposed a new model for predicting the effective permeation coefficient from the percolation path parameter.

$$K_e = \frac{\varepsilon}{\tau} \frac{\sum_{i=0}^{n}(d_i^2/32)(1+8\lambda/d_i)}{n} \tag{2}$$

Here, K_e is the effective permeation coefficient, ε is the porosity, τ is the average value of tortuosity factor, n is the number of percolation paths calculated in the analysis domain, d_i is the path size and λ is mean free path. The advantage of Eq (2) is that the empirical factor is not necessary, and every parameter can be determined for a 3D structure. For the porosity ε, the total porosity of the 3D structure can be applied. However, the total porosity includes the contribution of specific pores that do not contribute to gas flow, such as closed pores and side pocket type pores. Hence, applying total porosity for Eq (2) may overestimate the effective permeation coefficient. In order to extract only the pores contributing to the gas flow, effective porosity expressed by the following equation was proposed

$$\varepsilon_{eff} = \frac{\sum_{i=0}^{n}(\pi d_i^2 L_{path,i}/4)}{V_{total}} \tag{3}$$

where $L_{path,i}$ is the length of $path, i$ and V_{total} is the volume of the 3D structure for calculating the percolation path. Equation (3) assumes that only the path size controls the effective permeation coefficient (with the exception of the tortuosity factor). Although the influence of the pore size distribution in each path should be considered, Eq (3) is useful to determine the lower limit of the porosity. Therefore, in this study, the effective permeation coefficient calculated with Eq (2) has a specific range. The upper limit of the range is calculated with the total porosity, whilst the lower limit of the porosity is calculated with effective porosity. The calculated range is then compared with the effective permeation coefficient calculated by the CFD method. The results are shown in Fig. 9. Either the total porosity or the effective porosity is used, and a good correlation with the effective permeation coefficient calculated by the CFD method is obtained. For example, correlation factor between values calculated with Eq (2) and those calculated with CFD is calculated as 0.6. It should be noted that average value between the case of using total porosity and the case of using effective porosity was used for calculating correlation factor. With this result, the validity of our new model was verified.
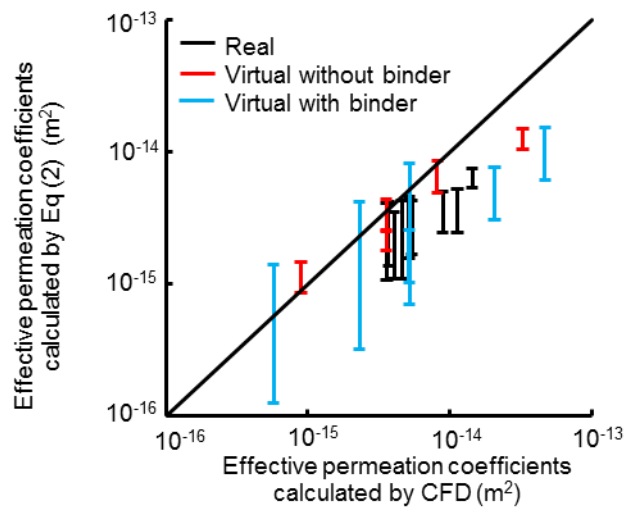

Fig. 9 Comparing effective permeation coefficient calculated with CFD and values calculated with Eq(2)

4. Conclusions

8 samples of real washcoat layers with different pore properties were used, and 12 virtual 3D structures simulating the pores of washcoat layers were computed. The secondary pores of the real washcoat layers were analyzed by SEM and synchrotron X-ray CT. The porosities obtained from X-ray CT were similar to those obtained from SEM. Hence, it was confirmed that the spatial resolution of X-ray CT was sufficient for the 8 samples used in this research. From the analysis of the pore properties for the real and computed 3D structures, a wide variation of pore properties was obtained: porosity, 20 to 32%; average pore size, 0.8 to 4 μm; path size of percolation path, 0.4 to 3 μm; average tortuosity factor, 1.3 to 1.6. Effective permeation coefficient was calculated using our proposed model and the obtained values were close to values calculated with CFD. Its correlation factor was 0.6. With these results, the validity of our proposed model to predict the effective permeation coefficient for the washcoat layer from the percolation path parameter was verified.

Reference

Carman. P.C., 1937, Fluid flow through granular beds, Transactions Institution of Chemical Engineers, 15, 150-166

Kato. S, Ozeki. H, Yamada. H, Tagawa. T, Takahashi. N, Shinjoh. H., 2013, Direct measurements of gas diffusivity in a washcoat layer under steady state conditions at ambient temperature, J. Ind. Eng. Chem, 19, 835-840

Kato. S, Ozeki. H, Yamada. H, Tagawa. T, Takahashi. N, Shinjoh. H., 2015a, Analysis of the Gas Diffusivity in the Simulated Washcoat Layer Based on Mean Transport Pore Model and the Mean Molecular Speed, Chemical Engineering Transactions, 43, 1591-1596

Kato. S, Ozeki. H, Yamada. H, Tagawa. T, Takahashi. N, Shinjoh. H, 2015b, Direct measurements of gas diffusivity in a washcoat layer under steady state and heated conditions, Chem. Eng. J, 271, 188-194

Kato. S, Yamaguchi. S, Tanabe. T, Nagai. Y, Yamada. H, Tomohiko Tagawa. T, 2017, Characterization of secondary pores in washcoat layers and their effect on effective gas transport properties, submitted in Chem. Eng. J

Kozeny. J., 1927, Ueber kapillare Leitung des Wassers im Boden, Sitzungsber Akad. Wiss., Wien, 136, 271-306

Hirose. Y, 2009, TOYOTA Beamline BL33XU, <http://www.spring8.or.jp/pdf/en/res_fro/09/170.pdf> accessed 06.01.2017

Miyakoshi. H, Sasaki. K, Hiramatsu. A., 1989, A Calculation Model for Gas Flow and Diffusion of a Porous Media with Pore Size Distribution, Material : Scientific and Technical Reports of the Mining College, Akita University Issue, 25,1-8

Nonaka. T, Dohmae. K, Hayashi. Y, Araki. T, Yamaguchi. S, Nagai. Y, Hirose. Y, Tanaka. T, Kitamura. H, Uruga. T, Yamazaki. H, Yumoto. H, Ohashi. H, Goto. S., 2016, Toyota beamline (BL33XU) at SPring-8, AIP Conf. Proc. 1741, 030043

Salejova. G, Grof. Z, Solcova, O, Schneider. P, Koseka. J., 2011, Strategy for predicting effective transport properties of complex porous structures, Computers and Chemical Engineering 35 200–211

Saiki. M, Matsunaga. S, Tsuji. R, Hachisuka. I, Senda. K., 2002, Koukai Tokkyo Koho JP 2002-191988 A